

Exploring compact binary populations with the Einstein Telescope

N.Singh,^{1*} T. Bulik,¹ K. Belczynski,² A. Askar³

¹ Astronomical Observatory, University of Warsaw, Al. Ujazdowskie 4, 00-478 Warsaw, Poland

² Nicolaus Copernicus Astronomical Center, Polish Academy of Sciences, ul. Bartycka 18, 00-716 Warsaw, Poland

³ Lund Observatory, Department of Astronomy, and Theoretical Physics, Lund University, Box 43, SE-221 00 Lund, Sweden

Received ; accepted

ABSTRACT

The Einstein Telescope (ET), a wide-band, future 3G gravitational wave detector, is to have expected detection rates of $\sim 10^5 - 10^6$ BBH detections and $\sim 7 \times 10^4$ BNS detections in one year. The coalescence of compact binaries with total mass 20 - 100 M_\odot , as typical of BH-BH or BH-NS binaries, will be visible up to redshift $z \approx 20$ and higher, thus facilitating the understanding of the dark era of the Universe preceding the birth of the first stars. The ET will therefore be a crucial instrument for population studies. We analysed the compact binaries originating in stars from (i) Pop I and Pop II, (ii) Pop III, and (iii) globular clusters, with single ET using the ET-D design sensitivity for the analysis. We estimate the constraints on the chirp mass, redshift and merger rate with redshift for these classes of compact object binaries. We conclude that ET as a single instrument is capable of detecting and distinguishing different compact binary populations separated in chirp mass - redshift space. The mass distributions characteristics of such different compact binary populations can also be estimated with single ET. Assuming that sufficient number of binaries will be detected from each of these populations, we also show that such populations are distinguishable in the combined bulk detection.

Key words. Gravitational waves; Stars: neutron, black holes; Methods: data analysis

1. Introduction

The Einstein Telescope (ET) is planned to have a detection sensitivity down to 1Hz (Hild et al. 2008; Hild 2012). It will thus have the ability to detect binary black holes (BBHs) of higher mass $10^2 - 10^4 M_\odot$ (Huerta & Gair 2011a,b; Gair et al. 2011; Amaro-Seoane & Santamaría 2010). ET will observe stellar mass binaries for a longer period of time in the detection band before their merger due to improved low-frequency sensitivity. By the end of the most recent O3 run, LIGO-Virgo has already tens of gravitational wave events in the GWTC-2 catalog (202 ????) and this number is expected to increase substantially in near future with the release of new results from the second half of the O3 run. The 3G detectors such as Einstein Telescope (ET) (Hild et al. 2011; Punturo et al. 2010) or Cosmic Explorer (CE) (Dwyer et al. 2015; Abbott et al. 2017; Reitze et al. 2019) will have an even higher detection rate (Maggiore et al. 2020). The expected detection rates are $\sim 10^5 - 10^6$ BBH detections and $\sim 7 \times 10^4$ BNS detections in one year (Regimbau et al. 2012, 2014; Belgacem et al. 2019), based on the ET-D (Hild et al. 2011) design sensitivity. Assuming that ET will have its design sensitivity, we investigate the prospects of using ET as a single instrument to analyze the capabilities of ET to detect and distinguish different compact binary populations.

In an earlier work (Singh & Bulik 2021a) we developed the algorithm for short duration gravitational wave signals from inspiralling compact binary system and estimated the area of localization for such short duration compact binary sources and also provided constraints on chirp mass, redshift, mass ratios. In the next algorithm (Singh & Bulik 2021b), we took into account the effect of rotation of the Earth on the antenna pattern function to analyse long duration signals from coalescing low mass com-

compact binary systems assuming the detector to be located at the Virgo site and proceeded by analysing the signal every 5 minutes assuming that the response functions for the three ET detectors does not change much within that period and estimated the constraints on the localization and the binary parameters such as chirp mass, total mass and redshift. We consider ET as a single detector rather than a part of network to detect the gravitational radiation from an inspiralling compact binary system in this analysis as in two previous works.

In the two preceding works (Singh & Bulik 2021a,b), we used a mock population assuming that the mass distribution is the same for all distances. We also assumed the distributions of masses, distances, locations in the sky, and polarizations to be independent. We assumed a uniform distribution in comoving volume and therefore did not take into account the dependence of the star formation rate (SFR) on redshift and the delay between formation and coalescence. Although such a population is not a realistic one, we choose such a simplified assumption in order to test the algorithm and to get an estimate of the accuracy of the recovered parameters. We proceed to analyse more realistic populations of compact binary systems originating from Pop I and Pop II, Pop III, and globular cluster populations in this work.

In this analysis, we consider multiple populations of compact binary systems with masses varying over a wide range and so expect the signal to stay in the ET detection band for a long duration. We use the algorithm developed for analysing such long duration signal (Singh & Bulik 2021b) to estimate the parameters such as chirp mass \mathcal{M} and redshift z of the compact binary systems. In §2 we describe the ET configuration, its antenna pattern function and the signal description. In §3 we describe the methodology used for this analysis while the details of the compact binary populations used to generate the mock population

* e-mail: nsingh@astrouw.edu.pl

sets are given in Sec 4. We present the results in §5 and the conclusions in §7.

2. Detection of compact binary coalescence with ET

We consider the ET triangular configuration consisting of three co-planar detectors, of equal arm length of 10 km, with an opening angle will be 60° . We assume ET to have the ET-D xylophone design (Hild et al. 2011) which is a realistic version of ET-C (Hild 2012) since it considers an improved noise model. Out of the multiple design configurations studied over time, ET-B (Hild et al. 2008) was the first basic design which was based on a single cryogenic interferometer and covered full frequency range of interest. The design was next updated to xylophone design resulting in the ET-C sensitivity (Hild 2012) in which each detector consisted of two interferometers, each with an opening angle of 60° . One interferometer was optimized for low frequencies while the other optimised for high frequencies. The single ET detector will thus have two interferometers, one each for low and high frequency. The final triangular design of the ET, will then have three such detectors, so six interferometers in total.

While observing a gravitational wave signal which stays in the detection band of the detector for a long duration, the change in the antenna response with the rotation of the Earth has to be taken into account. Following the detailed treatment of the antenna response given in (Jaranowski et al. 1998), which takes into account the motion of the Earth, the time dependent antenna response function for a single detector in the reference frame of the celestial sphere at time t is given as:

$$F_+(t) = \sin \eta [a(t) \cos 2\psi + b(t) \sin 2\psi] \quad (1a)$$

$$F_\times(t) = \sin \eta [b(t) \cos 2\psi - a(t) \sin 2\psi] \quad (1b)$$

where,

$$\begin{aligned} a(t) = & \frac{1}{16} \sin 2\gamma (3 - \cos 2\lambda)(3 - \cos 2\delta) \cos[2(\alpha - \phi_r - \Omega_r t)] \\ & - \frac{1}{4} \cos 2\gamma \sin \lambda (3 - \cos 2\delta) \sin[2(\alpha - \phi_r - \Omega_r t)] \\ & + \frac{1}{4} \sin 2\gamma \sin 2\lambda \sin 2\delta \cos[\alpha - \phi_r - \Omega_r t] \\ & - \frac{1}{2} \cos 2\gamma \cos \lambda \sin 2\delta \sin[\alpha - \phi_r - \Omega_r t] \\ & + \frac{3}{4} \sin 2\gamma \cos^2 \lambda \cos^2 \delta \end{aligned} \quad (2a)$$

and

$$\begin{aligned} b(t) = & \cos 2\gamma \sin \lambda \sin \delta \cos[2(\alpha - \phi_r - \Omega_r t)] \\ & + \frac{1}{4} \sin 2\gamma (3 - \cos 2\lambda) \sin \delta \sin[2(\alpha - \phi_r - \Omega_r t)] \\ & + \cos 2\gamma \cos \lambda \cos \delta \cos[\alpha - \phi_r - \Omega_r t] \\ & + \frac{1}{2} \sin 2\gamma \sin 2\lambda \cos \delta \sin[\alpha - \phi_r - \Omega_r t] \end{aligned} \quad (2b)$$

where, α, δ are the right ascension and the declination respectively, of the gravitational wave source. ψ is the polarization angle, λ is the latitude for the detector location and Ω_r is Earth's

rotational angular velocity. ϕ_r is the phase defining the position of the Earth in its diurnal motion at $t = 0$. The quantity $(\phi_r + \Omega_r t)$ is the local sidereal time at the detector site measured in radians. γ determines the orientation of the detector arms and is measured counter-clockwise from East to the bisector of the interferometer arms. η is the angle between the interferometer arms. $\eta = 60^\circ$ for ET in triangular configuration.

Using equations (1), the antenna response functions can be calculated for any given instant of time t . The location of ET detector for our analysis is chosen to be at the Virgo site.

According to general relativity, the two polarizations of the gravitational-wave produced by the gravitational-wave signal from an inspiraling compact binary system, have a monotonically-increasing frequency and amplitude with the orbital motion radiating gravitational wave energy. The two polarizations for $t < t_c$ of the waveform for a binary merging at a distance D_L , with the chirp mass \mathcal{M} described in Sec 3 of (Allen et al. 2012) are given as :

$$\begin{aligned} h_+(t) = & -\frac{1 + \cos^2 \iota}{2} \left(\frac{GM}{c^2 D_L} \right) \left(\frac{t_c - t}{5GM/c^3} \right)^{-1/4} \\ & \times \cos [2\Phi_c + 2\Phi(t - t_c; M, \mu)], \end{aligned} \quad (3a)$$

$$\begin{aligned} h_\times(t) = & -\cos \iota \left(\frac{GM}{c^2 D_L} \right) \left(\frac{t_c - t}{5GM/c^3} \right)^{-1/4} \\ & \times \sin [2\Phi_c + 2\Phi(t - t_c; M, \mu)], \end{aligned} \quad (3b)$$

where, c is the speed of light, G is the gravitational constant. ι is the angle of inclination of the orbital plane of the binary system w.r.t the observer. μ is the reduced mass of the binary system. The angle $\Phi(t - t_c; M, \mu)$ is the orbital phase of the binary system. For a binary system composed of component masses m_1 and m_2 , the chirp mass \mathcal{M} is given as $\mathcal{M} = (m_1 m_2)^{3/5} / M^{1/5}$, where $M = m_1 + m_2$ is the total mass. t_c and Φ_c are the time and phase respectively, of the termination of the waveform (Allen et al. 2012). The antenna response functions of one of the three detectors in ET, F_+, F_\times are defined in equation (1). Then the strain in the detector $h(t)$ is given as :

$$h(t) = F_+ h_+(t + t_c - t_0) + F_\times h_\times(t + t_c - t_0) \quad (4)$$

where t_0 is the time of coalescence in the detector frame and $(t_0 - t_c)$ is the travel of time from the source to the detector. The value of strain of the gravitational wave signal is obtained by substituting the values of the two polarizations from equation (3) in (4) :

$$\begin{aligned} h(t) = & -\left(\frac{GM}{c^2} \right) \left(\frac{\Theta}{4D_L} \right) \left(\frac{t_0 - t}{5GM/c^3} \right)^{-1/4} \\ & \times \cos [2\Phi_0 + 2\Phi(t - t_c; M, \mu)] \end{aligned} \quad (5)$$

where,

$$\Theta \equiv 2 \left[F_+^2 (1 + \cos^2 \iota)^2 + 4F_\times^2 \cos^2 \iota \right]^{1/2} \quad (6)$$

and,

$$2\Phi_0 = 2\Phi_c - \arctan \left(\frac{2F_\times \cos \iota}{F_+ (1 + \cos^2 \iota)} \right) \quad (7)$$

with $0 < \Theta < 4$. The antenna response functions are slowly varying functions of time. So in a given duration for which it can be assumed that the time of the signal in the detector bandwidth is short enough to ignore the change in the antenna response functions of the detector due to rotation of the Earth, the Fourier transform of the gravitational wave signal amplitude $h(t)$ in terms of frequency f is (Sathyaprakash & Dhurandhar 1991; Taylor & Gair 2012; O’Shaughnessy et al. 2010):

$$|\tilde{h}(f)| = \frac{2c}{D_L} \left(\frac{5G\mu}{96c^3} \right)^{1/2} \left(\frac{GM}{\pi^2 c^3} \right)^{1/3} \left(\frac{\Theta}{4} \right) f^{-7/6} \quad (8)$$

The signal to noise ratio (SNR) ρ_j for $j = (1, 2, 3)$ for each of the three ET detectors, obtained using match-filtering assuming that they have identical noise is given as (Taylor & Gair 2012; Finn 1996):

$$\rho_j \approx 8\Theta_j \frac{r_0}{D_L} \left(\frac{M_z}{M_{BNS}} \right)^{5/6} \sqrt{\zeta(f_{max})} \quad (9)$$

where $M_z = (1+z)M$ is the redshifted chirp mass and $M_{BNS} \approx 1.218M_\odot$ is the chirp mass of an equal mass binary with each component mass being $1.4M_\odot$.

$$\zeta(f_{max}) = \frac{1}{x_{7/3}} \int_1^{2f_{max}} \frac{df (\pi M_\odot)^2}{(\pi f M_\odot)^{7/3} S_h(f)} \quad (10)$$

where, $S_h(f)$ is the power spectral density (PSD) for ET-D configuration for the ET-D noise curve (Hild et al. 2011) and,

$$x_{7/3} = \int_1^\infty \frac{df (\pi M_\odot)^2}{(\pi f M_\odot)^{7/3} S_h(f)}. \quad (11)$$

The characteristic distance sensitivity r_0 is:

$$r_0^2 = \frac{5}{192\pi} \left(\frac{3G}{20} \right)^{5/3} x_{7/3} \frac{M_\odot^2}{c^3}, \quad (12)$$

The frequency at the end of the inspiral phase f_{max} , is given as:

$$f_{max} = 785 \left(\frac{M_{BNS}}{M(1+z)} \right) \text{ Hz} \quad (13)$$

where $M_{BNS} = 2.8M_\odot$ is the total mass of an equal mass binary with each component mass being $1.4M_\odot$. We can define the combined effective SNR for the combined signal from three detectors as:

$$\rho_{eff} = 8\Theta_{eff} \frac{r_0}{D_L} \left(\frac{M_z}{1.2M_\odot} \right)^{5/6} \sqrt{\zeta(f_{max})} \quad (14)$$

where the effective antenna response function Θ_{eff} is:

$$\Theta_{eff} = (\Theta_1^2 + \Theta_2^2 + \Theta_3^2)^{1/2}. \quad (15)$$

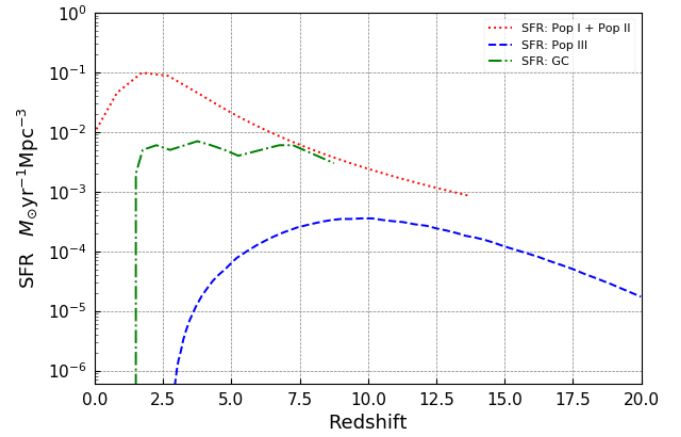


Fig. 1: The plot shows the star formation rate (SFR) used in the analysis for the Pop I and Pop II (Madau & Fragos 2017), Pop III (de Souza et al. 2011), and globular cluster population (Katz & Ricotti 2013).

3. Plan of the analysis

In this analysis, we consider multiple populations of compact binary systems with masses and redshifts, varying over a wide range and so the signal is expected to stay in the ET detection band for a long duration. We use the algorithm developed for analysing such long duration signals (Singh & Bulik 2021b) to estimate the parameters such as chirp mass M and redshift z of coalescing compact binary systems. The methodology of the analysis in this work is as follows:

- We consider compact binary systems from three sets of populations: (i) field binaries originating from population I and population II stars (Pop I and Pop II), (ii) binaries evolving in globular clusters (GC) and (iii) binaries from population III stars (Pop III). We construct a *mock population* of compact binary systems merging within Hubble time from each of these three population sets.
- The chirp mass and redshift of these *sources* are represented as $M_{s,mock}$ and $z_{s,mock}$ respectively.
- We assume that the ET detector is located at the Virgo site and has the ET-D design sensitivity.
- For every compact binary system, from each of the three sets of mock population, the gravitational wave signal in the ET detection band is split into 5 minute segments, from the time it enters the detection band at 1 Hz with f_{max} , the frequency at the end of the inspiral, limiting the duration of the last segment.
- The binary source is considered as *detected*, if it crosses a detection threshold set on the SNR.
- The chirp mass and redshift of these detected sources are represented as $M_{s,det}$ and $z_{s,det}$ respectively.
- The probability distribution for chirp mass and redshift for each detected source is estimated using the algorithm described in Singh & Bulik (2021b). (see fig 5 in Singh & Bulik (2021b) for an example).
- The median values of these estimated distributions of chirp mass and redshift for each detected compact binary source are represented as $M_{med,det}$ and $z_{med,det}$ respectively.

In this analysis we assume that in the case of detection of a coalescing binary system, the observables are as follows: (a)

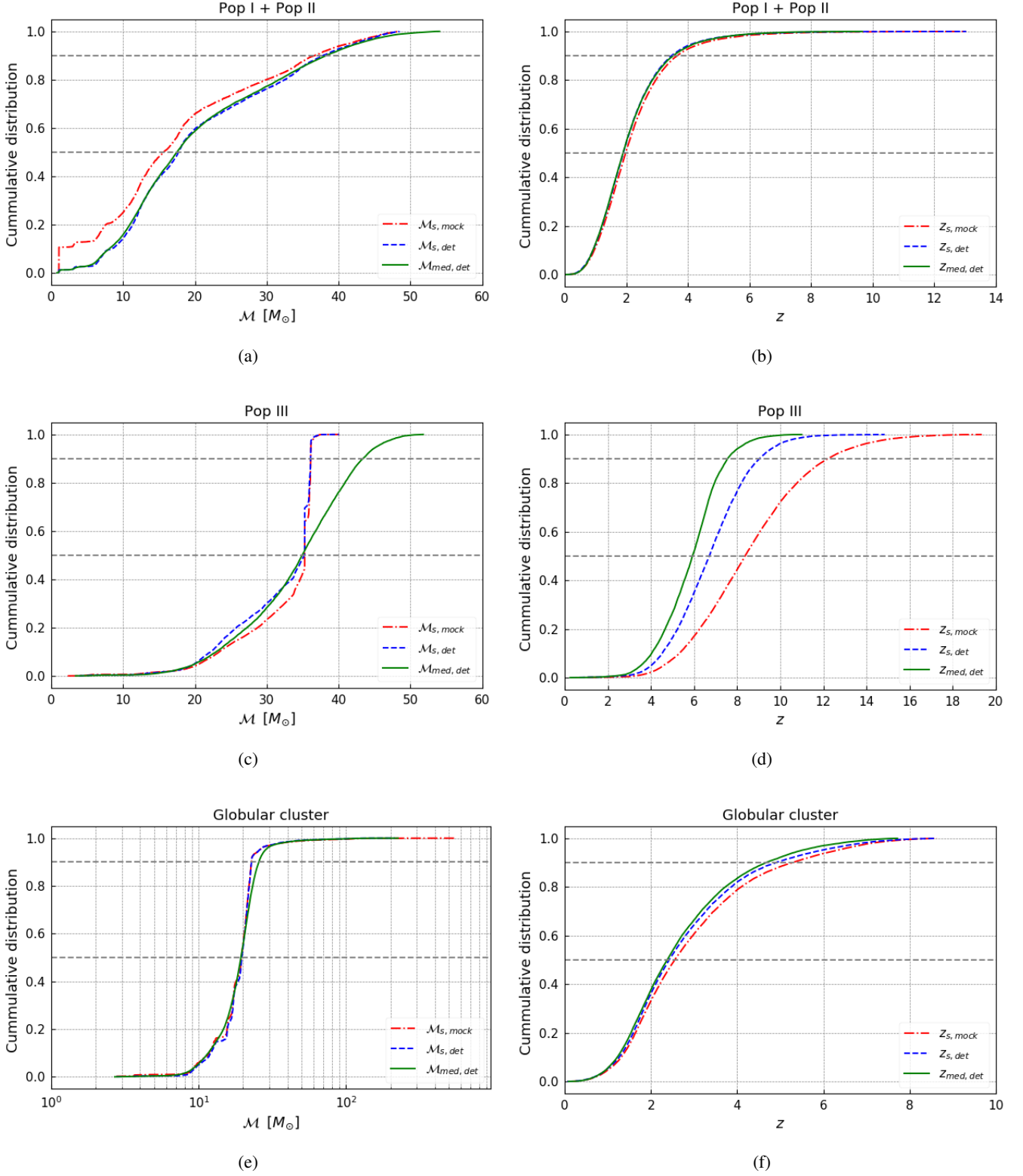


Fig. 2: The cumulative distribution of the parameters (left) \mathcal{M}_s and (right) z_s in the three populations. Top: Pop I and Pop II, middle: Pop III, and bottom: GC.

The three SNRs ρ_j^i defined by equation (9) for each i^{th} segment of the signal. (b) The phase of the strain $\Phi_{o,j}^i$ for $j = (1, 2, 3)$ corresponding to three detectors, defined in equation (7) for each i^{th} segment of the signal. The quantity Φ_0 is the best match

phase obtained by maximising the matched - filter output over the phase of the strain $h(t)$. The details are in Allen et al. (2012). (c) the gravitational wave frequency at the start and end of each segment of the detected signal. (d) The redshifted chirp mass

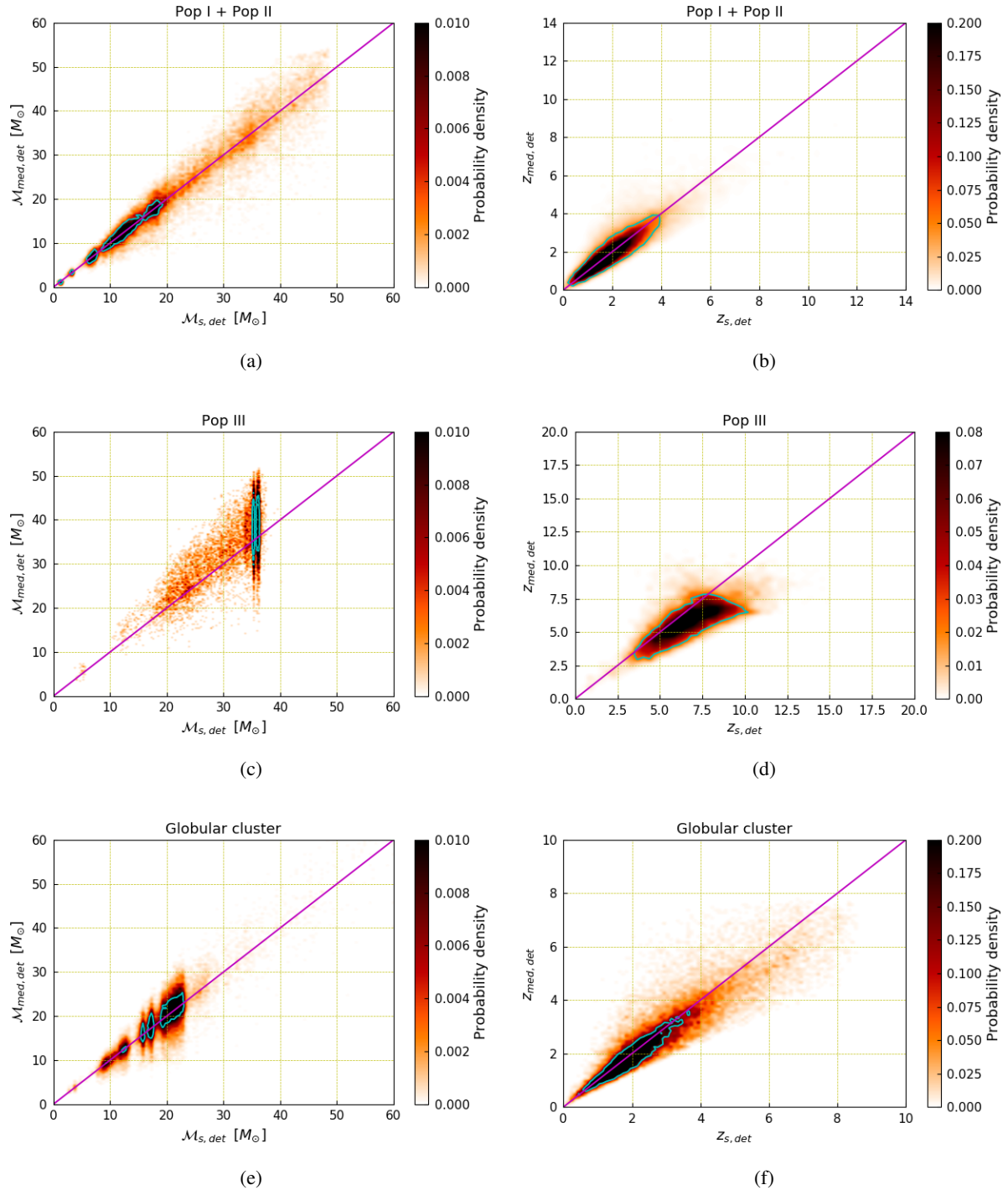


Fig. 3: The density distribution of the estimated median values w.r.t the actual values of the parameters (left) chirp mass \mathcal{M} and (right) redshift z of the detected compact binary sources. Top: Pop I and Pop II, middle: Pop III, and bottom: GC. The magenta line is a reference for equal values of actual and estimated parameters. The blue contour encloses the probability region of 90%.

\mathcal{M}_z . (e) The frequency at the end of the inspiral, corresponding to the innermost stable circular orbit, f_{max} .

Given the wide range of chirp masses the gravitational wave signal can stay in the ET detecting and for a long duration ranging from minutes to days, so we take into account the change in the antenna pattern with the rotation of the Earth. Following the algorithm described in (Singh & Bulik 2021b), we take into account the change in the antenna pattern due to the rotation of

the Earth and use the response function (Jaranowski et al. 1998) for the Celestial sphere frame of reference. Since antenna pattern is a slowly changing function of time, the change due to the rotation of Earth is negligible for a duration of 5 minutes. So we choose to analyse the signal every 5 mins. While the lowest frequency for the ET detection band is 1Hz, we fix the detection a threshold value of accumulated effective SNR $\rho_{eff} > 8$ and the SNR for i^{th} segment in the j^{th} detector $\rho_j^i > 3$ in at least one seg-

ment. for $j = (1, 2, 3)$ corresponding to the three ET detectors comprising single ET.

To construct a mock population of compact binaries originating for Pop I and Pop II stars we use the model M30.B generated by Belczynski et al. (2020) using an upgraded version of population synthesis code StarTrack (Belczynski et al. 2002, 2008). For compact binaries from Pop III stars, we use the model FS1 generated by (Belczynski et al. 2017). The globular cluster compact binaries population used in this analysis¹, was generated by (Askar et al. 2017).

3.1. Pop I and Pop II compact binaries

Belczynski et al. (2020) generated a broad set of models of compact binary systems with an upgraded version of population synthesis code StarTrack (Belczynski et al. 2002, 2008). We use the model M30.B to generate our population of compact binaries originating for Pop I and Pop II stars. The characteristic features of this model are described in detail in (Belczynski et al. 2020) and can be summarised as follows:

- Supernova engine model for NS/BH mass: This model uses a rapid supernova engine model as mentioned in (Fryer et al. 2012). It creates a mass gap in the range $(2 - 5)M_{\odot}$ between NSs and BHs. For this model minimum BH mass is assumed to be $2.5M_{\odot}$.
- Pair-instability supernovas and pair-instability pulsation supernova : This model allows pair-instability supernove (PSNs) for stars with He core mass in the range $(65 - 135)M_{\odot}$ thus entirely disrupting massive stars while for the low mass stars with He core mass in the range $(40 - 65)M_{\odot}$, it allows weak pair-instability pulsation supernovas (PPSNs) resulting in only up to 50% of mass loss calculated by (Leung et al. 2019), so that in this model, the maximum mass of post pair-instability pulsation supernovas star may reach $55.6M_{\odot}$.
- Neutrino mass loss: This model allows 1% neutrino mass loss to all BHs, while it allows 10% neutrino mass loss at NS formation.
- Natal kicks: This model assigns low natal BH kicks for low-mass BHs and no natal kicks for high-mass BHs. High kicks are assigned to neutron stars.
- Accretion: In this model it is assumed that 50% of mass lost by the donor during Roche lobe overflow (RLOF) is accreted on to the companion star if companion star in not a compact object. Accretion on compact objects (NSs or BHs) is allowed to be super-Eddington rate as presented by (Mondal et al. 2020). The 5% of Bondi-Hoyle rate accretion is allowed onto NS/BH during CE evolution.
- Winds: The model uses the massive star winds (Vink et al. 2001) in addition to Luminous Blue Variable (LBV) winds (Belczynski et al. 2010). It is assumed that LBV mass loss is independent of metallicity. In case of Wolf-Rayet (W-R) stars, the model assumes a prescription which is a combination of the Hamann & Koesterke (1998) wind rate estimate which takes into account W-R wind clumping, and Vink & de Koter (2005) wind metallicity-dependence.

This model is obtained from StarTrack site <http://www.syntheticuniverse.org/>, and contains result from 32 sim-

ulation of binary evolution with various metallicities Z_i where $i = (1 : 32)$. The metallicity grid values used in the model are :

$$Z = 0.0001, 0.0002, 0.0003, 0.0004, 0.0005, 0.0006, \\ 0.0007, 0.0008, 0.0009, 0.001, 0.0015, 0.002, 0.0025, \\ 0.003, 0.0035, 0.004, 0.0045, 0.005, 0.0055, 0.006, \\ 0.0065, 0.007, 0.0075, 0.008, 0.0085, 0.009, 0.0095, \\ 0.01, 0.015, 0.02, 0.025, 0.03. \quad (16)$$

Each simulation is done with the same initial conditions and is a result of simulating the same number (2 million) of massive binaries.

3.2. Pop III compact binaries

Belczynski et al. (2017) generated two models for the population of compact binary systems from the first, metal-free stars Pop III in the Universe using the population synthesis code StarTrack (Belczynski et al. 2002, 2008). They approximated the evolution of these Pop III stars with their metallicity model of

$$Z = 0.0001 \quad (17)$$

assuming no mass loss via stellar winds since mass loss in stellar wind is expected to be negligible for massive Pop III stars (Baraffe et al. 2001). The radial expansion of $Z = 0.0001$ metallicity model is constrained to match the upper limit of expansion of $Z = 0$ stars using the evolutionary model for Pop III stars calculated by (Marigo et al. 2001).

The initial conditions of the Pop III stars were defined based on the models obtained by (Ryu et al. 2016) using N-body simulation. Two models were chosen representing two different sizes of a gas cloud (mini-halo). These two models considered the formation of Pop III stars in mini halos of sizes ~ 2000 AU and $10 - 20$ AU respectively. For our analysis we use the results from the model FS1 (Belczynski et al. 2017) which assumes the formation of Pop III stars from a mini halo of size ~ 2000 AU (Stacy & Bromm 2013). Following the parameters specified by (Stacy & Bromm 2013) the number density of the gas medium is chosen to be 10^6cm^{-3} . The resulting population of metal-free binaries (initial mass function, mass ratio, orbital separations and eccentricities) are presented in detail in Belczynski et al. (2017). The population was taken from the <http://www.syntheticuniverse.org/> website which hosts the results of StarTrack simulations.

3.3. Globular cluster population

For data pertaining to merging BBHs produced by globular clusters, we made use of the results from MOCCA-Survey Database I (Askar et al. 2017). This database comprises about 2000 simulated globular cluster models that are characterized by different initial parameters. The long term evolution of these cluster models was carried out using the MOCCA code (Hypki & Giersz 2013; Giersz et al. 2013). For computing the dynamical evolution of a spherically symmetrical star cluster, the MOCCA code uses the orbit-averaged Monte Carlo treatment for relaxation (Hénon 1971; Stodolkiewicz 1986; Giersz 2001). For determining the outcome of binary-single and binary-binary encounters, it uses the FEWBODY code (Fregeau et al. 2004) which is a direct N -body integrator for small- N encounters. For stellar and binary evolution of stars, the version of MOCCA used in (Askar

¹ with the permission of Prof. M. Giersz

Table 1: Details of three population sets simulated for the analysis.

	Pop I & Pop II	Pop III	Globular cluster
N_{yr}	603147	34	36281
N_{mock}	25862	23990	26461
T_{mock} [yr]	0.04	705.59	0.73
N_{det}	20528	9683	22937
$(z_{min}, z_{max})_{mock}$	(0.03, 13.04)	(0.28, 19.36)	(0.06, 8.63)
$(M_{min}, M_{max})_{mock}$ [M_{\odot}]	(0.96, 48.47)	(2.27, 40.04)	(2.77, 554.63)

et al. 2017) utilized the prescriptions proved by the (SSE) and binary (BSE) codes (Hurley et al. 2000, 2002). MOCCA also uses realistic treatment for the escape process in tidally limited star clusters as described by (Fukushige & Heggie 2000).

The 2000 star clusters models in MOCCA-Survey Database I had different initial number of objects, metallicities, binary fractions, central densities, half-mass and tidal radii (see Table 1 in (Askar et al. 2017)). The initial stellar masses in these star cluster models are sampled from the IMF given by (Kroupa 2001) and have values between $0.08 M_{\odot}$ to $100 M_{\odot}$. For each initial model in the MOCCA-Survey Database I, two models were simulated with different prescriptions for BH natal kicks. In one case, the BH masses and natal kicks are computed using the mass fallback prescription from (Belczynski et al. 2002). In the other case, the BHs are given the same natal kicks as neutron stars which follow a Maxwellian distribution with $\sigma = 265 \text{ kms}^{-1}$ (Hobbs et al. 2005). The simulations assumed the metallicity values to be

$$Z = 0.0002, 0.001, 0.005, 0.006, 0.02 \quad (18)$$

corresponding to which 63, 831, 487, 64 and 503 models were simulated. The data for merging BBHs was taken from about 1000 of these models in which the mass fallback prescription from (Belczynski et al. 2002) was used to determine BH masses and natal kicks. The present-day observable properties of these stellar cluster models are broadly consistent with observed values for Galactic and extragalactic globular clusters (Askar et al. 2018; Leveque et al. 2021).

Askar et al. (2017) found 15134 coalescing BBHs that escape the clusters and 3000 BBHs that merged inside the cluster. The lower limit for the local merger rate of BBHs computed from these globular cluster simulations is $5.4 \text{ Gpc}^{-3} \text{ yr}^{-1}$. The cluster models simulated by (Askar et al. 2017) did not have the latest prescriptions for stellar evolution of BH progenitors connected with wind mass loss, pair/pulsational pair instability supernovae and the supernova engine model for NS/BH mass (see Section 3.1). For low metallicities, the maximum BH mass formed through single stellar evolution in (Askar et al. 2017) is about $30 M_{\odot}$. Additionally, these simulations do not take into account Post-Newtonian corrections during few-body encounters involving BHs. Such corrections can lead to gravitational wave capture or merger of BHs (Samsing et al. 2018; Rodriguez et al. 2018; Samsing 2018) inside star clusters. Despite, these shortcomings, the merger rates of merging BBHs from (Askar et al. 2017) are consistent with lower limits from newer globular cluster simulations in which these updates have been implemented (Kremer et al. 2020; Banerjee 2021; Mapelli et al. 2021).

3.4. Cosmological model

We assume flat cosmology, as done in the preceding chapters, with $\Omega_m = 0.3$, $\Omega_m + \Omega_{\Lambda} = 1$, $\Omega_k = 0$, $H_0 = 67.3 \text{ kms}^{-1} \text{ Mpc}^{-1}$ (Aubourg et al. 2015) and the relation between the luminosity

distance D_L and redshift z is obtained using the analytic approximation given by (Adachi & Kasai 2012). For this cosmology, the variation of comoving volume V_c with redshift z is given as,

$$\frac{dV}{dz} = 4\pi D_H \frac{D_L^2}{(1+z)^2 E_z}, \quad (19a)$$

where,

$$D_H = c/H_0 \text{ and } E_z = \sqrt{\Omega_m(1+z)^3 + (1-\Omega_m)} \quad (19b)$$

4. Mock source catalog

For generating the inspiraling compact binary sources originating for Pop I and Pop II population of stars, we begin with the StarTrack model M30.B (Belczynski et al. 2020). While the code can give us a lot of information about the binaries we will use only the following data for each binary: (i) the masses for the merging compact objects, (ii) the delay time between the formation of the binary and its coalescence and (iii) the metallicity of the binary.

A StarTrack population synthesis evolution (Belczynski et al. 2002, 2008) is done by simulating a number of binaries with a given initial distribution of parameters. This corresponds to a simulation of M_{sim} mass of stars, where one takes into account the binary fraction and the exact initial mass function for all stars and not just binaries.

The star formation rate SFR history is assumed following (Madau & Fragos 2017).

$$SFR(z) = 0.01 \left(\frac{(1+z)^{2.6}}{1 + ((1+z)/3.2)^{6.2}} \right) M_{\odot} \text{Mpc}^{-3} \text{yr}^{-1} \quad (20)$$

For generating the inspiraling compact binary sources originating for Pop III population of stars, we used the SFR given by (de Souza et al. 2011). The population of stars known as Pop III.2 are those zero-metallicity primordial stars which form in an initially ionized gas (Johnson & Bromm 2006; Yoshida et al. 2007). We use the SFR calculated for these Pop III.2 assuming the velocity of the metal-enriched galactic wind propagating outward from a central galaxy to be $v = 50 \text{ km/s}$ representing low chemical enrichment (de Souza et al. 2011).

(Katz & Ricotti 2013) found that most of the globular clusters present now formed during two distinct epochs of redshift $z \sim 2 - 3$ and at $z \gtrsim 6$ with $\sim 50\%$ of the total population having an estimated ages $\gtrsim 12 \text{ Gyr}$. They explored different assumptions on the minimum mass of the haloes in which proto-GC systems form. This corresponds to different assumptions on the minimum virial temperature T_{vir} of the host haloes in which GC systems are allowed to form. We use the GC formation rate, with

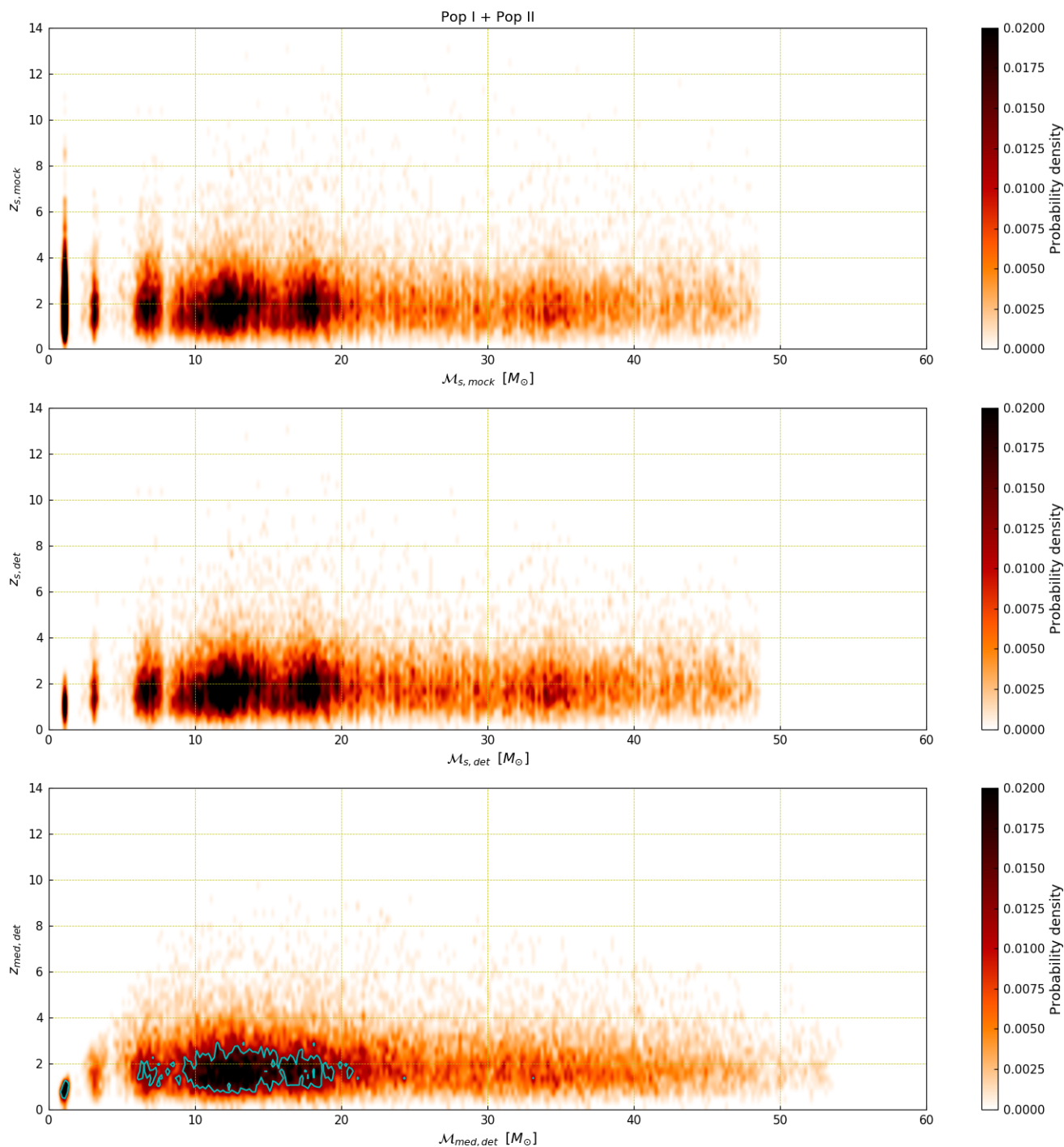


Fig. 4: The plots show the probability density of chirp mass and redshift in the $(\mathcal{M} - z)$ space for the three sets of parameters for Pop I and Pop II binaries. Top: the actual parameters of the sources in the mock population $\mathcal{M}_{s, mock}$ and $z_{s, mock}$. Middle: the actual parameters of the binaries which were detected $\mathcal{M}_{s, det}$ and $z_{s, det}$. Bottom: the estimated medians of the parameters for each of the detected compact binaries $\mathcal{M}_{med, det}$ and $z_{med, det}$. The blue contour encloses the probability region of 90% probability.

the assumption of $T_{vir} > 1.5 \times 10^5 \text{K}$ as shown in Figure 6 in Katz & Ricotti (2013).

Figure 1 shows the star formation rate dependence on redshift for the three population classes which we used to generate our mock populations. The red curve shows the SFR for Pop I and Pop II, obtained from (Madau & Fragos 2017). The SFR for Pop III obtained from (de Souza et al. 2011) is shown in blue

and the SFR for globular cluster formation shown in green is from (Katz & Ricotti 2013).

Additionally we have to take into account the evolution of metallicity with redshift which is given as (Madau & Fragos 2017):

$$Z = 0.02 \times 10^{0.153 - 0.074z^{1.34}} \quad (21)$$

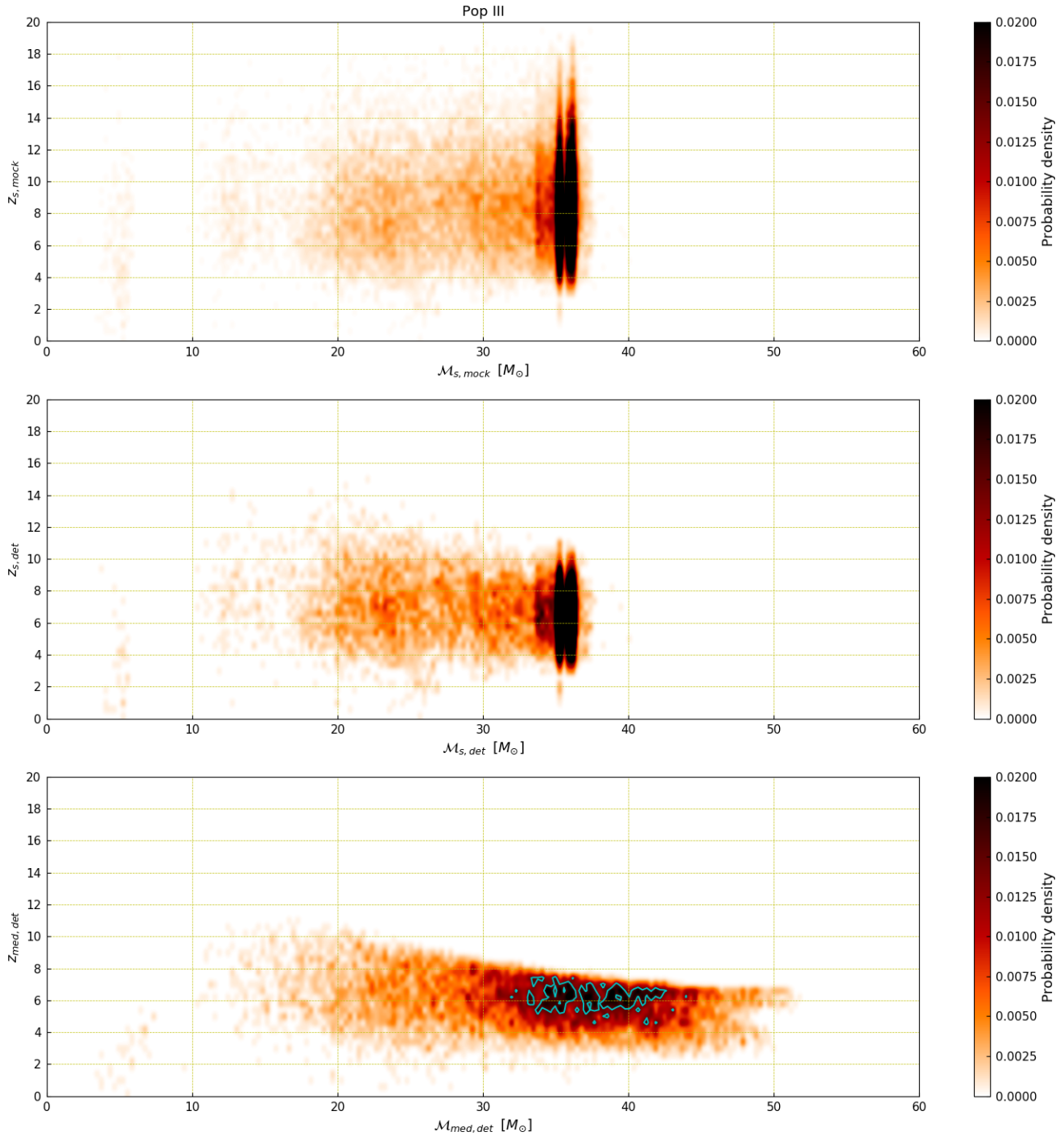


Fig. 5: The plots show the probability density of chirp mass and redshift in the $(\mathcal{M}-z)$ space for the three sets of parameters for Pop III binaries. Top: the actual parameters of the sources in the mock population $\mathcal{M}_{s, mock}$ and $z_{s, mock}$. Middle: the actual parameters of the binaries which were detected $\mathcal{M}_{s, det}$ and $z_{s, det}$. Bottom: the estimated medians of the parameters for each of the detected compact binaries $\mathcal{M}_{med, det}$ and $z_{med, det}$. The blue contour encloses the probability region of 90% probability.

For the purpose of this calculation we make a non-physical assumption that there is a one to one dependence of the metallicity on redshift. The function given in equation (21) can be easily inverted to obtain

$$z = \left[\frac{-\log(Z/0.02) + 0.153}{0.074} \right]^{1/1.34} \quad (22)$$

We use equation (22) to calculate the redshift intervals that correspond to a given metallicity. We assume that the stars are formed with this metallicity in a given redshift intervals. For the given grid we assume that the metallicity was constant and equal to Z_i in the redshift interval of z_{i-1} to z_i , as defined in §3 in equations

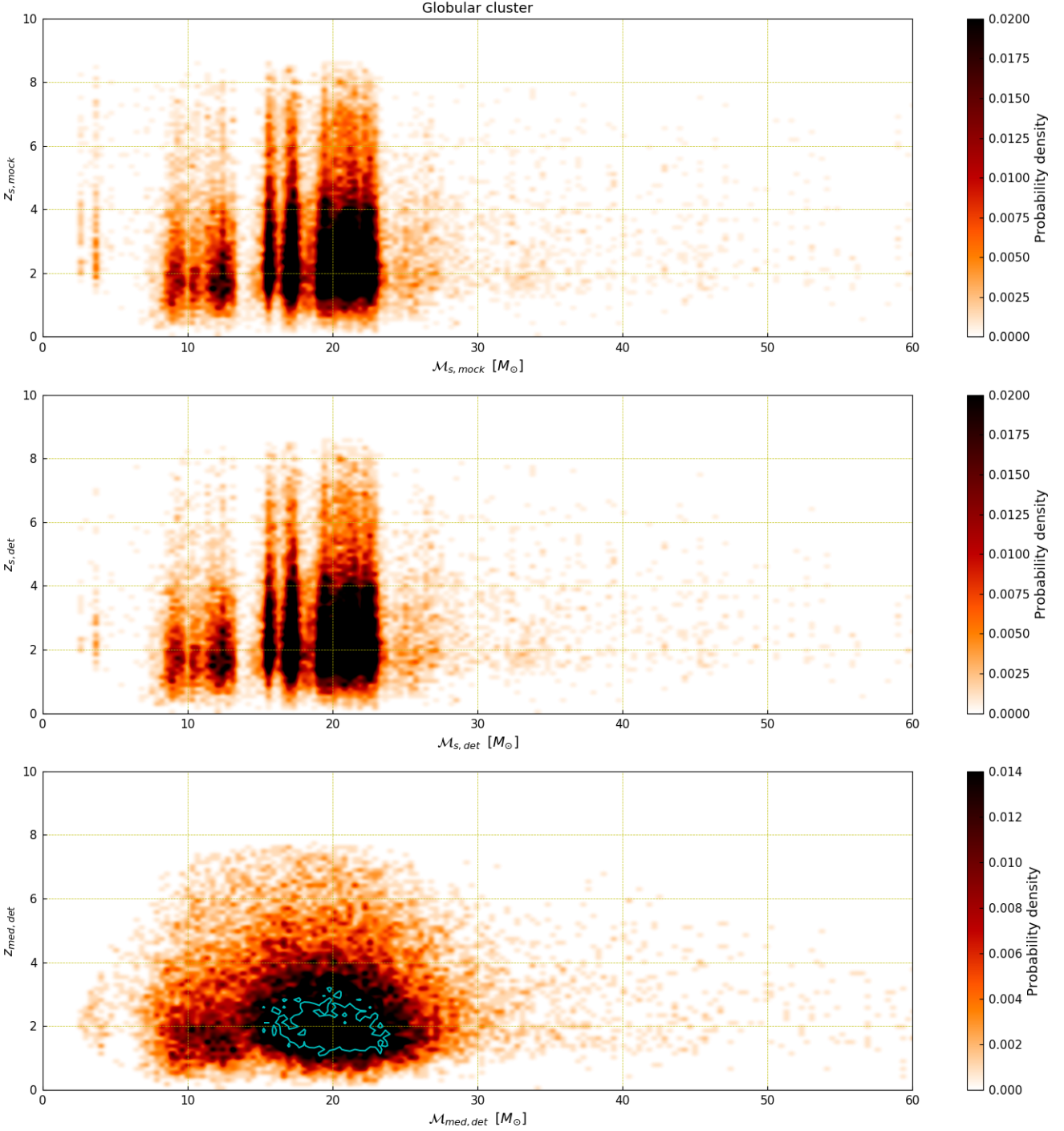


Fig. 6: The plots show the probability density of chirp mass and redshift in the $(M-z)$ space for the three sets of parameters for GC binaries. Top: the actual parameters of the sources in the mock population $\mathcal{M}_{s, mock}$ and $z_{s, mock}$. Middle: the actual parameters of the binaries which were detected $\mathcal{M}_{s, det}$ and $z_{s, det}$. Bottom: the estimated medians of the parameters for each of the detected compact binaries $\mathcal{M}_{med, det}$ and $z_{med, det}$. The blue contour encloses the probability region of 90% probability.

(16), (17) and (18). Thus the metallicity dependent star formation rate is

$$SFR(z, Z) = \begin{cases} SFR(z) & \text{if } z_{i-1}(Z) < z < z_i(Z) \\ 0 & \text{otherwise} \end{cases} \quad (23)$$

The simulations provide us with N binaries for which we have their masses $m_{1,2}^i$, delay times t_{del}^i , and metallicity Z_i . A

binary is formed at cosmic time t_{ini} corresponding to redshift $z_{ini} = z(t_{ini})$. It evolves for t_{evol} , and merges and $t_{del} = t_{evol} + t_{merg}$, where t_{evol} denotes the time from ZAMS to compact binary formation. This corresponds to the redshift $z_{del} = z(t_{del})$. The merger

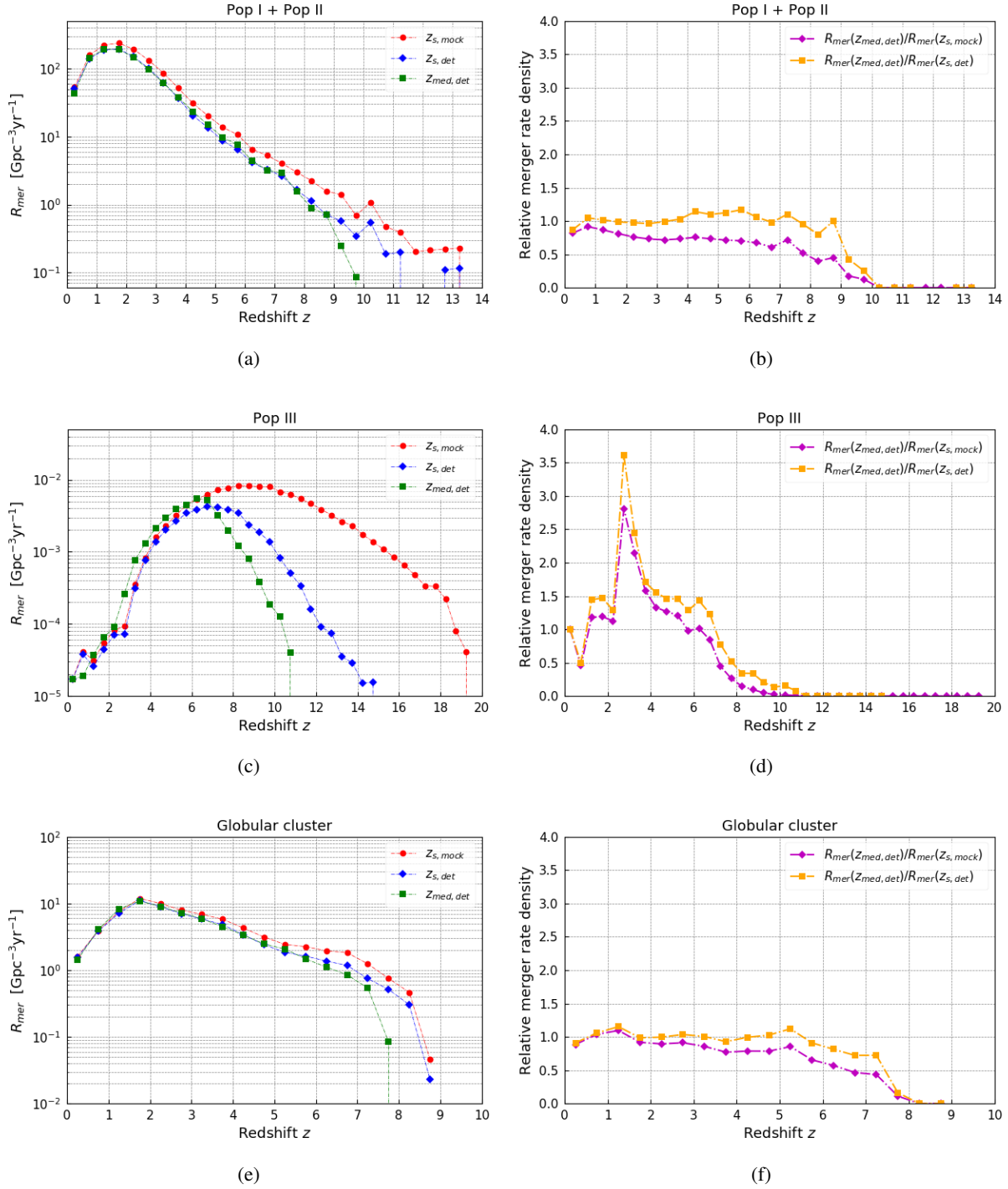


Fig. 7: The left panel shows the merger rate density for the duration T_{mock} , calculated for every 0.5 redshift bin. The right plot shows the relative merger rate density. Top: Pop I and Pop II, middle: Pop III, and bottom: GC.

rate density of given binary from the simulation as a function of redshift is given by

$$R_i(z) = \frac{1}{(1+z)} \frac{dV}{dz} \left(\frac{SFR(z(t(z_{ini}) + t_{evol}), Z)}{M_{sim}} \right) \quad (24)$$

We calculate the redshift dependence of the merger rate density of each binary and notice that the probability density of a

merger of a type i to happen in the Universe at redshift z is proportional to $R_i(z)$:

$$P(i, z) \propto R_i(z) \quad (25)$$

which is discrete in the index i and continuous in z . The probability distribution can be obtained by normalization.

We draw random binaries from the distribution given by equation (25) and obtain a synthetic population of mergers. Each

compact binary system drawn in this manner is then assigned a random values to the four angles: angle of declination δ , right ascension α , polarization angle ψ and inclination angle ι of the binary w.r.t the direction of observation. We choose $\cos \delta$, α/π , $\cos \iota$ and ψ/π , to be uncorrelated and distributed uniformly over the range $[-1, 1]$.

5. Results

Using the models for Pop I and Pop II, Pop III, and globular cluster compact binary object populations we generate the mock populations for our analysis. For all the three sets of mock compact binary population, we simulated N_{mock} , number of binaries. Out of these binaries, N_{det} are detected, based on the chosen detection threshold. Then the time during which these binaries in the mock population are expected to merger is

$$T_{mock} = N_{mock}/N_{yr} \text{ yr} \quad (26)$$

where N_{yr} is the expected number of mergers per year calculated by integrating the merger rate density given by equation (24).

In order to estimate the constraints on the chirp mass \mathcal{M} and redshift z , we follow the algorithm described in detail in (Singh & Bulik 2021b). Thus we get the probability distribution for chirp mass and redshift for each detected source. The median values of each of these estimated distributions of chirp mass and redshift for each detected compact binary source $\mathcal{M}_{med,det}$ and $z_{med,det}$ are then compared with the actual source parameters \mathcal{M}_s and z_s .

The merger rate density R_{mer} for each of the three mock populations is calculated for every redshift bin of 0.5 for the time T_{mock} of the simulation of the whole set of compact binary sources as:

$$R_{mer}(z_i, z_{i+1}) = \frac{N_{z_i:z_{i+1}}}{T_{mock}} \times \frac{dV}{dz} \quad (27)$$

where $N_{z_i:z_{i+1}}$ is the number of mergers in a redshift bin of ($z_i : z_{i+1}$).

In the mock population representing the population of compact binaries originating from Pop I and Pop II stars, we generate a set of 25862 sources. This corresponds to a time period of $T_{mock} = 0.04$ yr. The redshift of these sources range from $z_{min} = 0.03$ to $z_{max} = 13.04$ and the chirp mass is within the range $\mathcal{M}_{min} = 0.96M_{\odot}$ to $\mathcal{M}_{max} = 48.47M_{\odot}$.

From the population model of compact binaries from Pop III stars only, we obtain 23990 sources within the redshift range of $z_{min} = 0.28$ to $z_{max} = 19.36$ and the chirp mass range from $\mathcal{M}_{min} = 2.27M_{\odot}$ to $\mathcal{M}_{max} = 40.04M_{\odot}$. For this set of mock population, $T_{mock} = 705.59$ yr.

We generate 26461 compact binary sources from the globular cluster binary population corresponding to $T_{mock} = 0.73$ yr with the redshift range $z_{min} = 0.06$ to $z_{max} = 8.63$ and the chirp mass range from $\mathcal{M}_{min} = 2.77M_{\odot}$ to $\mathcal{M}_{max} = 554.63M_{\odot}$. The details of all the three mock populations are summarised in Table 1.

5.1. Mass and redshift estimates

Let us now compare the three sets of parameters: (i) the actual parameters of the sources in the mock population $\mathcal{M}_{s,mock}$ and $z_{s,mock}$, (ii) the actual parameters of the binaries which were detected $\mathcal{M}_{s,det}$ and $z_{s,det}$, and (iii) the estimated medians of the

parameters for each of the detected compact binaries $\mathcal{M}_{med,det}$ and $z_{med,det}$.

The cumulative distribution of the parameters in the three populations are shown on Figure 2. The top panel shows the Pop I and Pop II binaries, the middle panel shows the Pop III compact binary sources and the bottom panel shows the distributions for the globular cluster population of compact binaries. The red dot-dashed curve represents the distribution of the parameter value in a given mock population. The blue dashed curve represents the distribution of the parameter value of the detected binary systems out of a given mock population. The green solid curve represents the distribution of the estimated median of the parameter value.

The distribution for the parameters for the compact binaries originating from Pop I and Pop II stars is shown in Figures 2a and 2b. It shows that the binaries in this mock population are located up-to $z_{s,mock} \sim 13$, and this whole range of redshift is detectable. The estimated redshift of the detected binary sources for Pop I and Pop II population is $z_{med,det} \lesssim 10$. This shows that we underestimate the redshift for these binaries. Looking at the estimates of the chirp mass in Figure 2a, we see that the whole range of chirp masses is detectable but we overestimate the range of \mathcal{M} for this population of binaries to $\mathcal{M}_{med,det} \sim 55$.

In case of Pop III binaries, shown in Figures 2c and 2d, the mock population has sources with $\mathcal{M}_{s,mock} \lesssim 40M_{\odot}$ located up-to redshift $z_{s,mock} \sim 20$. The whole mass range of sources is detected for $z_{s,det} \lesssim 15$. We largely overestimate the range of chirp mass and underestimate the redshift of these detected sources to $\mathcal{M}_{med,det} \lesssim 52$ and $z_{med,det} \lesssim 11$.

Figures 2e and 2f show the distribution of parameters for the globular cluster binaries. It shows that the binaries over the whole range of redshift of $z_{s,mock} \sim 9$ are detectable but only masses with $\mathcal{M}_{s,det} \lesssim 215M_{\odot}$ are detectable. $\sim 99\%$ of the detected sources have $\mathcal{M}_{s,det} \lesssim 50M_{\odot}$. The chirp mass of the binaries of GC population is slightly overestimated while the redshift is slightly underestimated.

We now continue to compare the parameters of the detected binary sources. Figure 3 shows the 2D probability density distribution for the comparison between estimated median values ($\mathcal{M}_{median,det}$, $z_{median,det}$) w.r.t the actual values of the parameters ($\mathcal{M}_{s,det}$, $z_{s,det}$), for each detected compact binary source in a given population. The blue contour encloses the 90% of all the detected sources. The total number of detected sources in each mock population N_{det} is mentioned in Table 1. Chirp mass is shown in the left panel and redshift in the right panel.

Figures 3a and 3b show the probability density distribution \mathcal{M} and z for detected compact binaries from Pop I and Pop II stars. We see that for the 90% of the detected sources, which lie within $\mathcal{M}_{s,det} \lesssim 20M_{\odot}$ and $z_{s,det} \lesssim 4$, we have $\mathcal{M}_{median,det} \approx \mathcal{M}_{s,det}$ and $z_{median,det} \approx z_{s,det}$. The probability density peaks of $\mathcal{M}_{s,det}$ of the detected compact binaries in Pop I and Pop II population are mainly concentrated in five mass regions below $20M_{\odot}$ and are recovered correctly.

Figures 3c and 3d show the probability density distribution \mathcal{M} and z for detected compact binaries from Pop III stars. We see the two probability density peaks of $\mathcal{M}_{s,det}$ are correctly recovered but for the 90% of the detected sources, which lie within $35 \lesssim \mathcal{M}_{s,det}/M_{\odot} \lesssim 38$ and $3.5 \lesssim z_{s,det} \lesssim 10$, we have $\mathcal{M}_{median,det} \gg \mathcal{M}_{s,det}$ and $z_{median,det} \ll z_{s,det}$. Since most of the detected binaries are located at $3.5 \lesssim z_{s,det} \lesssim 10$, these generate a low SNR and hence have higher errors in the estimation of the parameters.

Figures 3e and 3f show the probability density distribution \mathcal{M} and z for detected compact binaries from stars evolving in the globular cluster. We see that regions of the five probability

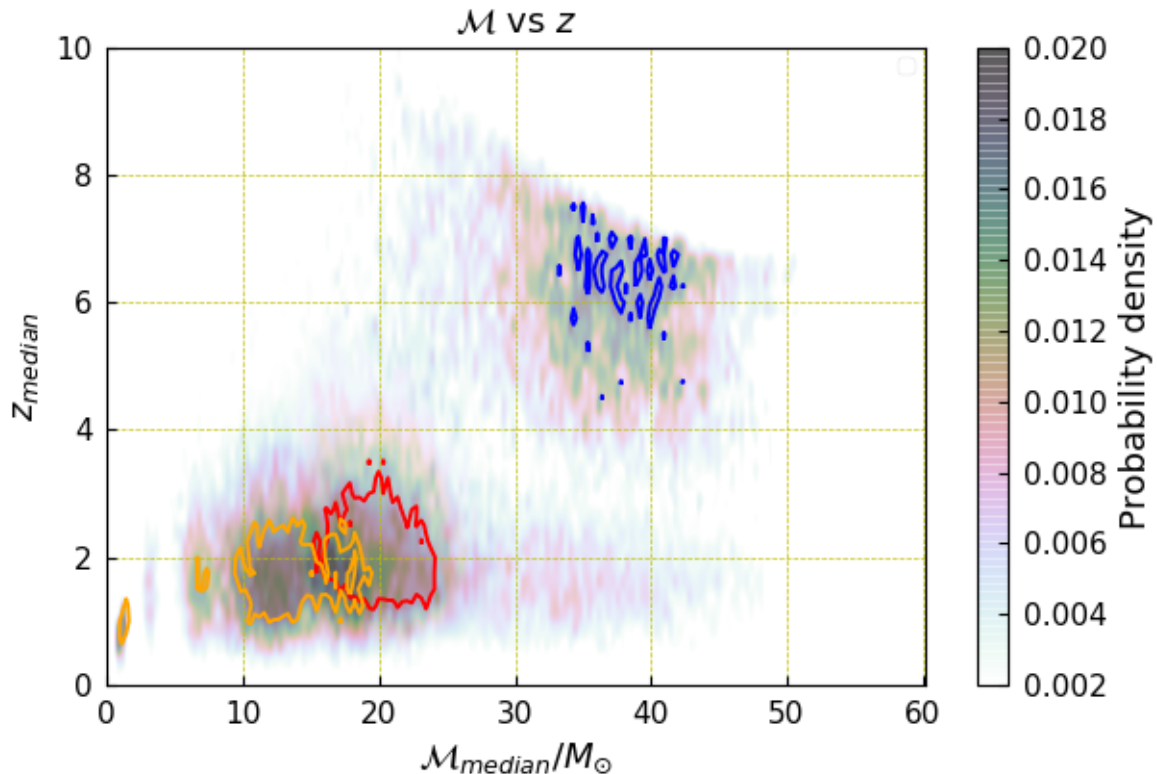


Fig. 8: The Pop I and Pop II, Pop III, and globular cluster population is plotted together with the contours showing the 90% region of each of the three set of populations. The orange contours enclose the 90% probability region of the recovered values of Pop I and Pop II binary population. The blue contours enclose the 90% Pop III population and the red contours enclose the 90% of globular cluster population. The density value shown in the color bar corresponds to the density values for each of three sets of the populations normalised individually.

density peaks of $\mathcal{M}_{s,det}$ are correctly recovered. For the 90% of the detected sources, which lie within $11 \lesssim \mathcal{M}/M_{\odot} \lesssim 25$ and $0.5 \lesssim z \lesssim 3.5$, we have $\mathcal{M}_{median,det} \gtrsim \mathcal{M}_{s,det}$ and $z_{median,det} \lesssim z_{s,det}$. It should be noted that the chirp mass distributions for the globular cluster data we used are sensitive to the prescriptions for evolution of BH progenitors. With different prescriptions such as rapid/delayed supernova, winds etc, these values could be higher and perhaps that might lead to better detectability and recovery of parameters.

Let us now consider the picture of the analysis in the $(\mathcal{M}-z)$ space, for the three sets of parameters: (i) the actual parameters of the sources in the mock population $\mathcal{M}_{s,mock}$ and $z_{s,mock}$, (ii) the actual parameters of the binaries which were detected $\mathcal{M}_{s,det}$ and $z_{s,det}$, and (iii) the estimated medians of the parameters for each of the detected compact binaries $\mathcal{M}_{med,det}$ and $z_{med,det}$. Figures 4, 5 and 6, show the 2D probability densities of the chirp mass and redshift of the compact binary systems for Pop I and Pop II, Pop III and globular cluster populations respectively.

In all the three figures, the top panel shows the parameters $\mathcal{M}_{s,mock}$ and $z_{s,mock}$, the middle panel shows the probability density of $\mathcal{M}_{s,det}$ and $z_{s,det}$ while the bottom panel shows the probability density the parameters $\mathcal{M}_{med,det}$ and $z_{s,det}$.

In Figure 4, we see that the probability density peaks in $\mathcal{M}-z$ are clearly visible in all three panels for the three sets of parameters but most of low mass sources $\mathcal{M} \lesssim 5M_{\odot}$ are not detected beyond redshift $z \approx 6$ and the redshift of the lighter binaries is underestimated. The blue contour encloses the region of 90%

probability for the estimated parameters $\mathcal{M}_{med,det}$ and $z_{med,det}$, of all the 20528 detected binaries.

Figure 5 shows the 2D probability density in the $(\mathcal{M}-z)$ space for the Pop III compact binary sources. The probability density of $\mathcal{M}-z$ is seen to peak in two close regions in the limit $35 \lesssim \mathcal{M}_{s,mock}/M_{\odot} \lesssim 38$ for $2 \lesssim z \lesssim 20$ and are detectable within a redshift range of $2 \lesssim z \lesssim 12$. As noted earlier, the low SNR generated by these sources result in a larger error on the estimated parameter values. Due to this, the redshift is largely underestimated while the chirp mass is largely overestimated. We can thus see that the features of mass distributions for the Pop III binary systems are not recovered accurately and a refined population model should be considered for further analysis. The blue contour encloses the region of 90% probability for the estimated parameters $\mathcal{M}_{med,det}$ and $z_{med,det}$, of all the 9683 detected binaries.

The 2D probability density in the $(\mathcal{M}-z)$ space for the globular cluster compact binary sources is shown in Figure 6. Most of the detectable lighter binaries with $\mathcal{M}_{s,det} \lesssim 5M_{\odot}$ are within $z \approx 7$. There is an underestimation of the redshift of the binaries detected beyond $z \approx 1$, as seen earlier in Figure 3f, which results in the overestimation of the chirp mass of these binaries. The blue contour encloses the region of 90% probability for the estimated parameters $\mathcal{M}_{med,det}$ and $z_{med,det}$, of all the 22937 detected binaries.

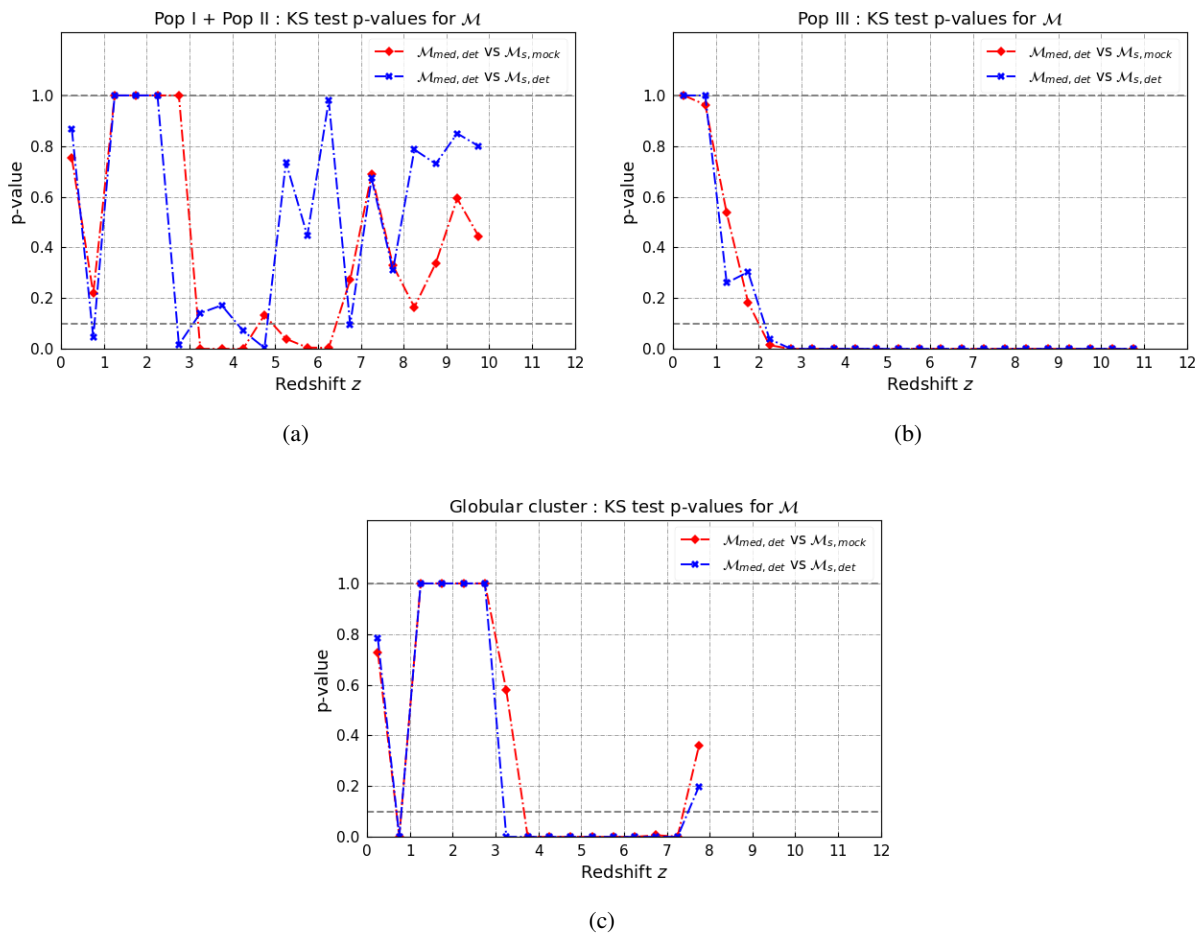


Fig. 9: The plots show the p-values for the chirp mass, calculated for the binary sources of Pop I and Pop II, Pop III, and globular cluster populations in redshift bin of 0.5.

5.2. Estimates of the merger rates

We estimate the merger rate density $R_{mer}(z)$ for the time duration T_{mock} , for every 0.5 redshift bin using equation (27). We bin the redshift values of all the binary sources in a given mock population $z_{s,mock}$ to obtain the number of binaries in the given redshift bin, and then using (27), obtain $R_{mer}(z_{(s,mock)_i}, z_{(s,mock)_{i+1}})$. Thus we get $R_{mer}(z_{s,mock})$. The merger rates $R_{mer}(z_{s,det})$ and $R_{mer}(z_{med,det})$ are calculated similarly. We also calculate the relative merger rate densities $\frac{R_{mer}(z_{med,det})}{R_{mer}(z_{s,mock})}$ and $\frac{R_{mer}(z_{med,det})}{R_{mer}(z_{s,det})}$ for comparison.

The results are shown in the Figure 7. The left panel shows $R_{mer}(z)$ and the right panel shows the corresponding relative merger rate densities. The top, middle and bottom panels show the estimates for Pop I and Pop II binaries, Pop III and the globular cluster population of compact binaries.

Figures 7a and 7b show the rate estimates for the Pop I and Pop II compact binaries. $R_{mer}(z_{s,det})$ and $R_{mer}(z_{med,det})$ are in good agreement for redshift $z \lesssim 8.75$. For larger redshifts the deviation tends to increase.

The merger rate estimates for Pop III compact binary systems are shown in Figures 7c and 7d. The large underestimation of higher redshift values results in $R_{mer}(z_{med,det}) \gg R_{mer}(z_{s,det})$ for $2 \lesssim z \lesssim 6$ and $R_{mer}(z_{med,det}) \ll R_{mer}(z_{s,det})$ for $z \gtrsim 7$.

Figures 7e and 7f show the rate estimates for the globular cluster compact binaries. $R_{mer}(z_{s,det})$ and $R_{mer}(z_{med,det})$ are

in good agreement for redshift $z \lesssim 7.5$. At higher redshifts, $R_{mer}(z_{med,det}) \ll R_{mer}(z_{s,det})$

6. Recovered mass distributions

We analysed the parameters such as chirp mass \mathcal{M} , redshift z , and the merger rate of the inspiraling compact binary systems of Pop I and Pop II, Pop III, and globular cluster population using a single ET. In order to see the distinguishability of each population we plot all of them in Figure 8. The normalization of each of the three sets : Pop I and Pop II, Pop III, and globular cluster depends on the merger rates of each of these populations. We generate the 2D density for each set and normalize them individually. We calculate the 90% probability region for $\mathcal{M} - z$ values in each of these three sets of populations.

In Figure 8, the orange contours enclose the 90% probability region of the recovered values of Pop I and Pop II binary population. The blue contours enclose the 90% Pop III population and the red contours enclose the 90% of globular cluster population. The three regions are clearly distinguishable.

Each population of compact binary system is characterised by a specific $\mathcal{M} - z$ distribution. Although the full space of these parameters for each set of populations has been shown, we now proceed with the analysis of the recovered chirp mass values in every redshift bin of 0.5. We compare the values of $\mathcal{M}_{med,det}$ and $\mathcal{M}_{s,det}$ and also compare $\mathcal{M}_{med,det}$ and $\mathcal{M}_{s,mock}$, with Kol-

mogorov–Smirnov (KS) test in order to see the recovery of the features in chirp mass distribution for each of the three mock population sets.

These comparisons are shown in Figures 9a, 9b and 9c.

For the compact binary sources originating from Pop I and Pop II stars, shown in top panel, the comparison in each redshift bin shows that $p \geq 10\%$ for the full redshift range except for $z \approx 0.75$ and for the range $2.75 \leq z \leq 6.75$. Thus the null hypothesis cannot be rejected except in this range. The p-values for binaries from Pop III population, shown in the middle panel, show that $p \geq 10\%$ for $z \leq 2$. In the case for binaries from globular cluster, $p \leq 10\%$ for $z \approx 0.75$ and for the range $3.25 \leq z \leq 7.25$.

7. Conclusion

We analysed the compact binary populations of (i) Pop I and Pop II, (ii) Pop III, and (iii) globular clusters, with single ET using the ET-D design sensitivity for the analysis. The three sets of populations represent different metallicities and hence different age of the binary population and represent different formation scenarios. Thus the analysis presents the capability of single ET to detect and distinguish different compact binary populations. We took into account the effect of rotation of the Earth on the antenna pattern and estimated the parameters chirp mass \mathcal{M} , redshift z , and merger rate R_{mer} for each of the three sets of the populations. We show if the populations of compact binaries are separated in $\mathcal{M} - z$ space, then ET as a single instrument is capable of detecting and distinguishing these different compact binary populations. If the populations overlap in $\mathcal{M} - z$, then it will be necessary to consider other parameters such as spin to estimate the distinguishability.

It was found that based on the chosen detection threshold, 90% of the detected Pop I and Pop II binaries lie within $z \leq 3.5$, Pop III up to $z \leq 9$ and globular cluster binaries up to $z \leq 5$. The deviation of the estimated values of the chirp mass, redshift and merger rate density as compared with the actual source values of these parameters for the detected binaries, is much larger in the case of Pop III as compared to that in the case of Pop I and Pop II, and the globular cluster binaries. Since the features of mass distributions for the Pop III binary systems are not recovered accurately, a detailed analysis with refined population model should be taken into consideration to recover the correct distribution for this population of compact binaries.

Assuming that sufficient number of binaries are detected from each of these populations it was also shown that, the three sets of populations are distinguishable in the combined bulk detection.

We checked accuracy of the the recovery of the chirp mass for each redshift bin of 0.5 in each of the population sets with KS test. For the Pop I and Pop II compact binary sources, the null hypothesis cannot be rejected except for the range the range $2.75 \leq z \leq 6.75$. However in the case Pop III population the p-value $\geq 10\%$ only for $z \leq 2$ while in the case of globular cluster population p-value $p \leq 10\%$ for $z \approx 0.75$ and for the range $3.25 \leq z \leq 7.25$. We thus find that that the mass distributions characteristics of different compact binary populations can be estimated with single ET.

Acknowledgements. NS and TB are thankful to Prof. Mirek Giersz for permitting the use of MOCCA data. N.S and T.B acknowledge the support from the Foundation for Polish Science grant TEAM/2016-3/19 and NCN grant UMO-2017/26/M/ST9/00978. AA acknowledges support from the Swedish Research Council through the grant 2017-04217. This document has been assigned Virgo document number VIR-0785A-21.

References

- ????
- Abbott, B. P., Abbott, R., Abbott, T. D., et al. 2017, *Classical and Quantum Gravity*, 34, 044001
- Adachi, M. & Kasai, M. 2012, *Progress of Theoretical Physics*, 127, 145
- Allen, B., Anderson, W. G., Brady, P. R., Brown, D. A., & Creighton, J. D. E. 2012, *Phys. Rev. D*, 85, 122006
- Amaro-Seoane, P. & Santamaría, L. 2010, *ApJ*, 722, 1197
- Askar, A., Arca Sedda, M., & Giersz, M. 2018, *MNRAS*, 478, 1844
- Askar, A., Szkudlarek, M., Gondek-Rosińska, D., Giersz, M., & Bulik, T. 2017, *MNRAS*, 464, L36
- Aubourg, É., Bailey, S., Bautista, J. E., et al. 2015, *Phys. Rev. D*, 92, 123516
- Banerjee, S. 2021, arXiv e-prints, arXiv:2108.04250
- Baraffe, I., Heger, A., & Woosley, S. E. 2001, *ApJ*, 550, 890
- Belczynski, K., Bulik, T., Fryer, C. L., et al. 2010, *ApJ*, 714, 1217
- Belczynski, K., Kalogera, V., & Bulik, T. 2002, *ApJ*, 572, 407
- Belczynski, K., Kalogera, V., Rasio, F. A., et al. 2008, *ApJS*, 174, 223
- Belczynski, K., Kléncki, J., Fields, C. E., et al. 2020, *A&A*, 636, A104
- Belczynski, K., Ryu, T., Perna, R., et al. 2017, *MNRAS*, 471, 4702
- Belgacem, E., Dirian, Y., Foffa, S., et al. 2019, *J. Cosmology Astropart. Phys.*, 2019, 015
- de Souza, R. S., Yoshida, N., & Ioka, K. 2011, *A&A*, 533, A32
- Dwyer, S., Sigg, D., Ballmer, S. W., et al. 2015, *Phys. Rev. D*, 91, 082001
- Finn, L. S. 1996, *Phys. Rev. D*, 53, 2878
- Fregeau, J. M., Cheung, P., Portegies Zwart, S. F., & Rasio, F. A. 2004, *MNRAS*, 352, 1
- Fryer, C. L., Belczynski, K., Wiktorowicz, G., et al. 2012, *ApJ*, 749, 91
- Fukushige, T. & Hoggie, D. C. 2000, *MNRAS*, 318, 753
- Gair, J. R., Mandel, I., Miller, M. C., & Volonteri, M. 2011, *General Relativity and Gravitation*, 43, 485
- Giersz, M. 2001, *MNRAS*, 324, 218
- Giersz, M., Hoggie, D. C., Hurley, J. R., & Hypki, A. 2013, *MNRAS*, 431, 2184
- Hamann, W. R. & Koesterke, L. 1998, *A&A*, 335, 1003
- Hénon, M. 1971, *Ap&SS*, 13, 284
- Hild, S. 2012, *Classical and Quantum Gravity*, 29, 124006
- Hild, S., Abernathy, M., Acernese, F., et al. 2011, *Classical and Quantum Gravity*, 28, 094013
- Hild, S., Chelkowsky, S., & Freise, A. 2008, arXiv e-prints, arXiv:0810.0604
- Hobbs, G., Lorimer, D. R., Lyne, A. G., & Kramer, M. 2005, *MNRAS*, 360, 974
- Huerta, E. A. & Gair, J. R. 2011a, *Phys. Rev. D*, 83, 044020
- Huerta, E. A. & Gair, J. R. 2011b, *Phys. Rev. D*, 83, 044021
- Hurley, J. R., Pols, O. R., & Tout, C. A. 2000, *MNRAS*, 315, 543
- Hurley, J. R., Tout, C. A., & Pols, O. R. 2002, *MNRAS*, 329, 897
- Hypki, A. & Giersz, M. 2013, *MNRAS*, 429, 1221
- Jaranowski, P., Królak, A., & Schutz, B. F. 1998, *Phys. Rev. D*, 58, 063001
- Johnson, J. L. & Bromm, V. 2006, *MNRAS*, 366, 247
- Katz, H. & Ricotti, M. 2013, *MNRAS*, 432, 3250
- Kremer, K., Ye, C. S., Rui, N. Z., et al. 2020, *ApJS*, 247, 48
- Kroupa, P. 2001, *MNRAS*, 322, 231
- Leung, S.-C., Nomoto, K., & Blinnikov, S. 2019, *ApJ*, 887, 72
- Leveque, A., Giersz, M., & Paolillo, M. 2021, *MNRAS*, 501, 5212
- Madau, P. & Fragos, T. 2017, *ApJ*, 840, 39
- Maggiore, M., Van Den Broeck, C., Bartolo, N., et al. 2020, *J. Cosmology Astropart. Phys.*, 2020, 050
- Mapelli, M., Bouffanais, Y., Santoliquido, F., Arca Sedda, M., & Artale, M. C. 2021, arXiv e-prints, arXiv:2109.06222
- Marigo, P., Girardi, L., Chiosi, C., & Wood, P. R. 2001, *A&A*, 371, 152
- Mondal, S., Belczyński, K., Wiktorowicz, G., Lasota, J.-P., & King, A. R. 2020, *MNRAS*, 491, 2747
- O’Shaughnessy, R., Kalogera, V., & Belczynski, K. 2010, *ApJ*, 716, 615
- Punturo, M., Abernathy, M., Acernese, F., et al. 2010, *Classical and Quantum Gravity*, 27, 194002
- Regimbau, T., Dent, T., Del Pozzo, W., et al. 2012, *Phys. Rev. D*, 86, 122001
- Regimbau, T., Meacher, D., & Coughlin, M. 2014, *Phys. Rev. D*, 89, 084046
- Reitze, D., Adhikari, R. X., Ballmer, S., et al. 2019, in *Bulletin of the American Astronomical Society*, Vol. 51, 35
- Rodriguez, C. L., Amaro-Seoane, P., Chatterjee, S., et al. 2018, *Phys. Rev. D*, 98, 123005
- Ryu, T., Tanaka, T. L., & Perna, R. 2016, *MNRAS*, 456, 223
- Samsing, J. 2018, *Phys. Rev. D*, 97, 103014
- Samsing, J., Askar, A., & Giersz, M. 2018, *ApJ*, 855, 124
- Sathyaprakash, B. S. & Dhurandhar, S. V. 1991, *Phys. Rev. D*, 44, 3819
- Singh, N. & Bulik, T. 2021a, *Phys. Rev. D*, 104, 043014
- Singh, N. & Bulik, T. 2021b, arXiv e-prints, arXiv:2107.11198
- Stacy, A. & Bromm, V. 2013, *MNRAS*, 433, 1094
- Stodolkiewicz, J. S. 1986, *Acta Astron.*, 36, 19
- Taylor, S. R. & Gair, J. R. 2012, *Phys. Rev. D*, 86, 023502
- Vink, J. S. & de Koter, A. 2005, *A&A*, 442, 587
- Vink, J. S., de Koter, A., & Lamers, H. J. G. L. M. 2001, *A&A*, 369, 574
- Yoshida, N., Oh, S. P., Kitayama, T., & Hernquist, L. 2007, *ApJ*, 663, 687